Energy 196 (2020) 117090

Contents lists available at ScienceDirect

Energy

journal homepage: www.elsevier.com/locate/energy

Robust design optimization (RDO) of thermoelectric generator system using non-dominated sorting genetic algorithm II (NSGA-II)

Ungki Lee [a], Sudong Park [b], Ikjin Lee [a, *]

[a] Department of Mechanical Engineering, Korea Advanced Institute of Science and Technology, Daejeon, 34141, South Korea
[b] Energy Conversion Research Center, Korea Electrotechnology Research Institute, Changwon, 51543, South Korea

ARTICLE INFO

Article history:
Received 27 July 2019
Received in revised form
21 November 2019
Accepted 2 February 2020
Available online 5 February 2020

Keywords:
Thermoelectric generator (TEG)
Robust design optimization (RDO)
Uncertain parameter
Non-dominated sorting genetic algorithm II
Surrogate model
Global sensitivity analysis

ABSTRACT

The thermoelectric generator (TEG) is a promising technology for the exhaust heat recovery of automobiles and TEG optimization has been widely studied. However, previous TEG optimization studies did not consider variations in the TEG net power output caused by uncertain parameters in the TEG system. This paper introduces a robust design optimization (RDO) that maximizes the mean of the performance function while minimizing its variance, leading to an optimum design that is less sensitive to uncertainties in TEG systems. A surrogate model is used to reduce the computational cost and the non-dominated sorting genetic algorithm II (NSGA-II) is used to find a compromise solution. The standard deviation of the TEG net power output of the deterministic optimum design (93.51W) verifies that the uncertainty of TEG systems significantly affects the variation of the TEG net power output, indicating that the uncertainty should be considered in TEG optimization problems. The compromise solution guarantees stable and high TEG net power output compared to the deterministic optimum design stemming from existing TEG optimization studies. The results of a global sensitivity analysis using the Sobol index indicate that the inlet temperature of the hot fluid has the greatest impact on the TEG net power output.

1. Introduction

The increase in the number of automobiles has brought greater convenience; however, concerns about environmental pollution, fossil-fuel depletion, and global warming have increased at the same time [1]. For a typical internal combustion engine, discharging heat to the atmosphere is necessary to complete the thermodynamic process, and 40% of the energy from the fuel is discharged in the form of exhaust gas [2]. When waste heat is efficiently reused, energy efficiency can be increased and the environment can be improved by reducing these types of gaseous emissions [3]. The thermoelectric generator (TEG), which uses solid-state energy conversion technology that directly generates electricity from waste heat via the Seebeck effect, is considered to be a very useful waste heat recovery technique [4]. TEGs are environmentally friendly because they do not emit gases or pollutants, and there is less concern about wear given their lack of moving parts [5]. Therefore, many automotive manufacturers have studied TEGs to improve the fuel efficiency by generating useful electricity from the waste heat in the exhaust gases. Domingues et al. [6] evaluated the potential of using the thermal energy of vehicle exhaust gas through a Rankine cycle system. They noted that the thermal and mechanical efficiency rates can be improved by increasing the evaporating pressure of the working fluid. Zhang et al. [7] demonstrated the recovery of exhaust waste heat from an automotive diesel engine using a nanostructured TEG. Lan et al. [8] developed a dynamic model of a TEG system intended to recover the waste heat of a vehicle. They concluded that the model can be used for model-based control design. Nithyanandam and Mahajan [9] improved the heat transfer performance of a TEG for automobiles using a heat exchanger based on metal foam. They reported that their TEG with metal foam has 6–8 times higher net electric power output than a TEG without metal foam. Muralidhar et al. [10] developed a waste-heat recovery model for hybrid electric vehicles using a TEG. Zhao et al. [11] proposed an intermediate fluid TEG system for automobile waste heat recovery and reported that a uniform temperature distribution of a module in their study can be obtained with their system. Many studies of TEG optimization have been conducted to improve the low efficiency of TEGs and to propose an effective TEG system modeling method. Deng et al. [12]

* Corresponding author.
E-mail addresses: lwk920518@kaist.ac.kr (U. Lee), john@keri.re.kr (S. Park), ikjin.lee@kaist.ac.kr (I. Lee).

https://doi.org/10.1016/j.energy.2020.117090
0360-5442/

Nomenclature

A	area of a P—N couple (m^2)
c	specific heat capacity ($Jg^{-1}K^{-1}$)
D	hydraulic diameter (m)
f	Darcy resistance coefficient
f_z	pressure drop (Pa)
h	convective heat transfer coefficient ($Wm^{-2}K^{-1}$)
H	exchanger height (m)
I	electric current (A)
K	thermal conductance (WK^{-1})
k	total heat transfer coefficient ($Wm^{-2}K^{-1}$)
L	length of exchanger (m)
m	total mass flow rate (gs^{-1})
n_x	number of P—N couple in the direction of fluid flow
n_y	number of P—N couple in row
Nu	Nusselt number
P	power (W)
Q	total heat quantity (W)
q	heat quantity (W)
R	electrical resistance (Ω)
R_{cont}	contact thermal resistance (m^2KW^{-1})
T	temperature (K)
t	thickness (mm)
U	total electromotive force (V)
v	flow velocity (ms^{-1})
W	exchanger width (m)

Greek symbols

α	Seebeck coefficient (VK^{-1})
λ	thermal conductivity ($Wm^{-1}K^{-1}$)
ρ	density (kgm^{-3})

Subscripts

cf	cold fluid
ci	inlet cold fluid
cs	cold-side surface of TEG
cer	ceramic plate
con	connector
exc	exchanger plate
hf	hot fluid
hi	inlet hot fluid
hs	hot-side surface of thermoelectric module
int	internal value
load	load value
net	net value
pn	P—N semiconductor couple
pump	pump value
TEG	TEG module value

performed experiments and simulations with a thermoelectric generator based on automotive exhaust gas and reported the optimized shape of a heat exchanger. Liang et al. [13] presented a two-stage thermoelectric model and obtained an optimum thermocouple ratio that maximizes the output power. Su et al. [14] optimized the heat exchanger to obtain a uniform temperature distribution and higher interface temperature. Kumar [15] demonstrated the optimal design of a thermoelectric module and TEG designs by solving the heat flux and temperature variations in the thermoelectric legs. Kempf et al. [16] used heat exchanger optimization strategies to optimize the parameters of a heat exchanger and the configuration of the TEG system by considering the trade-off between the fuel efficiency losses and the power output of the TEG. Chen et al. [17] derived an optimized geometry of TEG elements using a multi-objective genetic algorithm (MOGA). They concluded that the MOGA is a useful approach for industrial applications and for designing geometries that maximize TEG performance capabilities. Marvão et al. [18] optimized the dimensions of a TEG for heavy-duty freight vehicles and identified critical parameters of the optimization process.

During the TEG optimization studies above, the objective was to maximize the TEG net power, which is the difference between the generated electrical power and the power loss in the pump, or the COP (coefficient of performance) of the device. However, uncertainties in TEG systems lead to large variations in the objective functions of the TEG optimization problem, and a given design may not achieve the intended optimal performance outcomes [19]. There are various uncertain parameters that affect the variation of the TEG performance outcomes, such as the inlet temperatures of the fluids [20], the mass flow rate [21], the Seebeck coefficient [22], and the electrical resistivity [23], and these parameters deserve consideration when optimizing a TEG. Currently, the stochastic characteristics of engineering systems are commonly considered when solving problems related to optimization [24]. Youn et al. [25] established the reliability-based optimum design of a vehicle by considering the uncertainty of a side impact model of the vehicle. Shin and Lee [26] optimized the roadway radius and speed limit design by considering probabilistic characteristics associated with how the vehicle was driven. Lee et al. [27] considered the uncertainty of Li-ion batteries and the driving characteristics in the optimization of the design of an electric vehicle. These studies demonstrated that system failures can occur with a deterministic optimum design derived by optimization without considering the uncertainties. While most existing TEG optimization problems focus on finding a deterministic optimum design, the importance of finding a stochastic optimum design is currently emerging. Therefore, this study starts with the idea of applying an optimization method that considers not only the TEG performance but also variations of the performance caused by uncertainties in the TEG system to ensure high and stable TEG performance without large fluctuations during the actual TEG operation.

Robust design optimization (RDO), which is one of the multi-objective optimizations, is an approach that increases the quality of a product by reducing the variability in the output performance function by finding an optimal design which is insensitive to uncertain factors in the decision variables and parameters [28]. RDO has been widely applied to many engineering research fields. Kang and Bai [29] investigated the RDO of truss structures with unknown and bounded parameters. Fang et al. [30] applied RDO to improve the performance and robustness of the fatigue life of a truck cab. They used dual surrogate models for the surrogate modeling of the fatigue life and demonstrated that the fatigue life of the optimum design can be improved such that it is less sensitivity to uncertainties. Tammareddi et al. [31] used the multi-objective particle swarm optimization approach to minimize the effects of uncertainties on the optimal design of a coronary stent. Wu et al. [32] proposed an adaptive stochastic optimization framework and performed robust aerodynamic shape optimization for drag minimization. Kang et al. [33] utilized robust topology optimization for multi-material structures while taking into account material interface-related uncertainties. In the RDO approach, the objective function and the product quality can be expressed by the first two statistical moments — the mean and variance — of the output performance function [34]. The statistical moments can be estimated by sampling methods such as Monte Carlo simulation (MCS) [35] or the Latin hyper cube sampling (LHS) method [36]. Because the objective function of RDO includes both the mean and variance of the performance function, and the optimization proceeds with the goals of increasing the mean and decreasing the variance, it is expected to derive a design that can guarantee high and stable TEG performance under uncertainties when applied to TEG optimization problems.

Therefore, the main objective of the paper is to study an optimal heat exchanger design that ensures high and stable TEG net power under actual operation by considering uncertain factors in the TEG system model for the recovery of automobile exhaust gas waste heat with the RDO approach. The heat exchanger design is important because it directly affects the TEG net power by determining the pressure drop and the amount of heat transferred to the TEG module. In the RDO formulation step, the weight of the mean and variance of the performance function are included in the objective function, with the optimal design varying depending on the weight setting. This paper uses the non-dominated sorting GA II (NSGA-II), which derives a set of optimal solutions during multi-objective optimization by finding solutions that are not dominated by others to obtain a Pareto set consisting of optimal solutions and to determine a compromise solution from the Pareto set. In addition, a global sensitivity analysis is conducted to select the uncertain parameters to be carefully examined by assessing the impact of the uncertain parameters on TEG performance.

In this paper, in order to decrease the computational burden of the optimization process, a surrogate model that is used in various design optimization problems is applied to provide an approximation of the TEG system model. Zhang et al. [37] undertook the aerodynamic and structural optimization of a high-subsonic transport aircraft wing using surrogate models to reduce the computation time for optimization. Samad et al. [38] employed a weighted-average surrogate model during the shape optimization of a rectangular channel to improve the heat transfer properties. Li et al. [39] presented an adaptive optimization method based on the Kriging surrogate model and efficiently optimized the structure of a stent and the length of a stent dilatation balloon. MCS is also used to estimate statistical moments of the TEG net power output by randomly generating samples from the statistical distributions of decision variables or parameters, as the process is easy to perform and accurate with a large sample size.

The remainder of this paper is composed as follows. Section 2 explains the system optimization framework including the TEG system model, the surrogate modeling process, and the uncertainties in the TEG system model. In Section 3, the methodologies of the robust design optimization process, NSGA-II, and the global sensitivity analysis are presented. Section 4 presents and discusses the results of the study. Finally, Section 5 summarizes the findings and suggests directions for future research.

2. Optimization framework

As shown in Fig. 1, the proposed RDO framework for the TEG system consists of four major steps: 1) TEG system modeling, 2) surrogate modeling to replace the TEG system model, 3) RDO to consider uncertainties in the TEG system, and 4) a global sensitivity analysis to identify influential input parameters. Sections 2.1 and 2.2 present a description of the TEG system model and the theoretical background and validation of the generated surrogate model, respectively. Section 2.3 depicts the uncertainties of the TEG system model used for RDO. Detailed explanations of the RDO process and the global sensitivity analysis are given in Section 3.

2.1. Thermoelectric generator (TEG) system model

This paper uses a TEG system model, the structure of which includes a sandwich-shaped plate-type exhaust heat exchanger, as presented by He et al. [40]. A thermoelectric module can generate electricity using the temperature difference between hot and cold fluid channels. An Illustration of the TEG system is depicted in Fig. 2. The hot fluid with waste heat flows to the channel in the middle and heats the thermoelectric element, and the cooling fluid at a low temperature flows to the upper and lower channels and acts as a heat sink to cool the thermoelectric element on the other side. The TEG system consists of two thermoelectric modules, with the hot and cold fluids flowing in identical directions. Because they have symmetrical structures and operate under the identical conditions, it is assumed that the two modules perform identically. The cooling water of the engine flows into coolant exchangers with a total mass flow rate of $m_{cf} = 500\text{gs}^{-1}$ and inlet temperature of $T_{ci} = 353.15\text{K}$. The convective heat transfer coefficient of the cold water is assumed to be constant with a value of $h_{cf} = 1000\text{Wm}^{-2}\text{K}^{-1}$ along the longitudinal direction of the exchanger. The inlet temperature and total mass flow rate of the hot fluid are $T_{hi} = 873.15K$ and $m_{hf} = 40\text{gs}^{-1}$, respectively.

A finite element analysis is used for each TEG module to

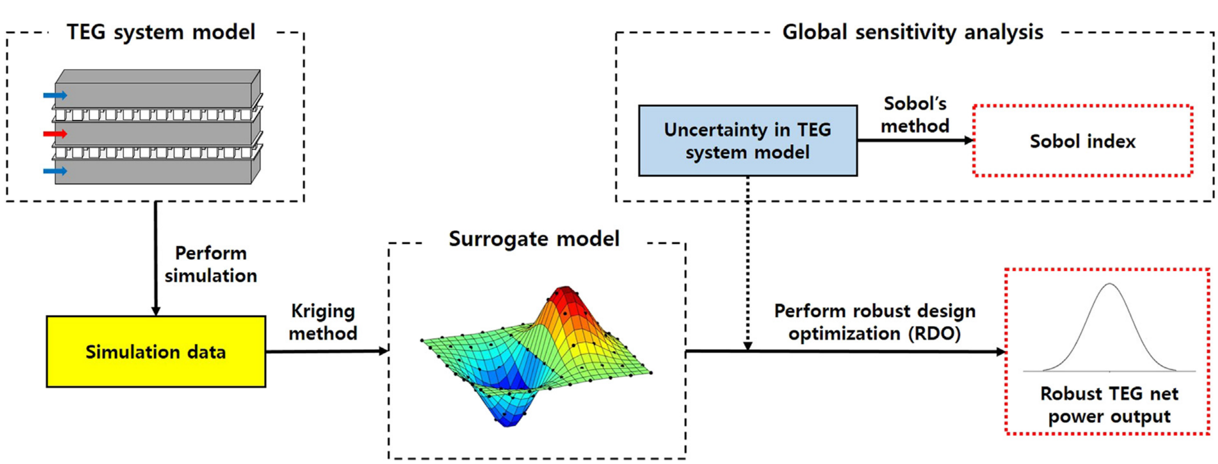

Fig. 1. RDO process for the TEG system optimization.

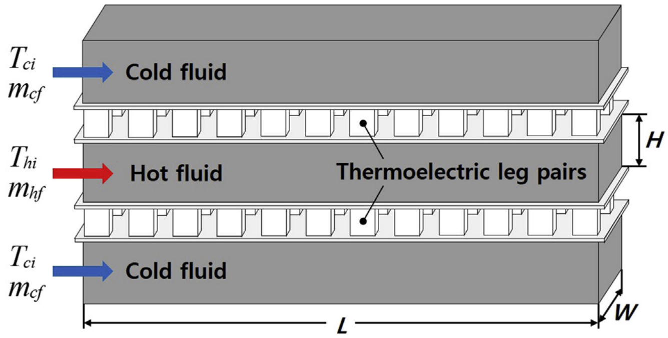

Fig. 2. Illustration of the TEG system.

determine the temperature distribution in the direction of the fluid flow caused by the heat transfer from the hot to the cold fluids. Calculation particles $n_x \times n_y$ in size constitute the TEG module, with a single pair of P—N semiconductors considered as a unit and with the location of each calculation particle expressed as coordinates (i, j). Assuming that there is no temperature difference between the thermoelectric elements in the width direction, each line of thermoelectric elements containing n_y P—N elements can serve as a new calculation unit. As presented in Fig. 3, copper connectors connect in series a p-n junction, which consists of bismuth-telluride (Bi_2Te_3), and ceramic plates (Al_2O_3) are utilized in the thermal conduction and electrical insulation processes. In the finite element model of the TEG module, T_{cf}, T_{hf}, T_{cs}, and T_{hs} indicate the temperatures of the cold fluid, exhaust fluid (hot fluid), cold-side surface, and hot-side surface of thermoelectric module, respectively. Given that the outlet temperatures in the ith unit – T_{cf}^{i+1} and T_{hf}^{i+1} – are used as the inlet temperatures in the $(i+1)^{th}$ unit, the temperatures are calculated sequentially. The following basic assumptions of the TEG system model are used in this paper [41]: the external load resistance (R_{load}) of the TEG module is identical to the total internal resistance of the TEG module; the Thomson effect, all radiative heat transfers, and the conductive heat transfer along the longitudinal direction of the exchangers are neglected; no space exists between the thermoelectric legs; all P- or N-type semiconductor materials have constant thermoelectric properties and identical physical properties; copper is the materials used for both the hot-side and cold-side heat exchanger plates; and the hot-side and cold-side contact thermal resistances between the TEG module and the exchanger plate are identical.

Basic equations and parameters associated with the TEG system model are presented in Tables 1 and 2, respectively. Sequential quadratic programming (SQP) is employed to solve coupled equations related to the temperature distribution of the TEG module surface, the electric current (I), and the total heat transfer coefficient of the hot side (k_{hf}). The mathematical problem for solving the coupled equations can be formulated as

$$\underset{I_0,\ k_{hf0}}{\operatorname{argmin}} |I - I_0| + \left|k_{hf} - k_{hf0}\right|, \tag{1}$$

where I_0 and k_{hf0} are the initial guess of the electric current and the total hot-side heat transfer coefficient; I is calculated from the distribution of the TEG module surface temperature using the given values of I_0 and k_{hf0}; and k_{hf} can also be calculated from the obtained temperature distribution of the TEG module surface.

2.2. Surrogate modeling

2.2.1. Kriging method

During the simulation-based optimization process, function evaluations with a simulation model are used to find an optimum solution, and an approximation of the simulation model is often necessary given that a heavy computational cost is involved. Because TEG system model simulations are time-consuming, an approximate model that can replace the simulation model is necessary to perform RDO efficiently. A surrogate model is a model that approximates the simulation model and is also known as a metamodel. The Kriging method involves the building of a surrogate model assuming that a regression model and a stochastic process comprise a response function [42]. For response function $Y(\mathbf{x}_i)$ at n sample points, $\mathbf{X} = [\mathbf{x}_1,\ \mathbf{x}_2, \ldots,\ \mathbf{x}_n]^{\mathrm{T}}$ with $\mathbf{x}_i \in \mathbf{R}^{nr}$, the response can be expressed as

$$\mathbf{Y} = \mathbf{F}\boldsymbol{\beta} + \mathbf{e}, \tag{2}$$

where $\mathbf{Y} = [Y(\mathbf{x}_1),\ Y(\mathbf{x}_2), \ldots, Y(\mathbf{x}_n)]^{\mathrm{T}}$ with $Y(\mathbf{x}_i) \in \mathbf{R}^1$ represents n responses; $\mathbf{F} = [f_p(\mathbf{x}_i)]$, $i = 1, \ldots, n$, $p = 1, \ldots, P$ is an $n \times P$ design matrix; $f_p(\mathbf{x})$ denotes regression functions that consist of polynomial basis functions; $\mathbf{F}\boldsymbol{\beta}$ is the response mean structure; $\boldsymbol{\beta} = [\beta_1,\ \beta_2, \ldots,\ \beta_P]^{\mathrm{T}}$ is an unknown regression coefficient vector;

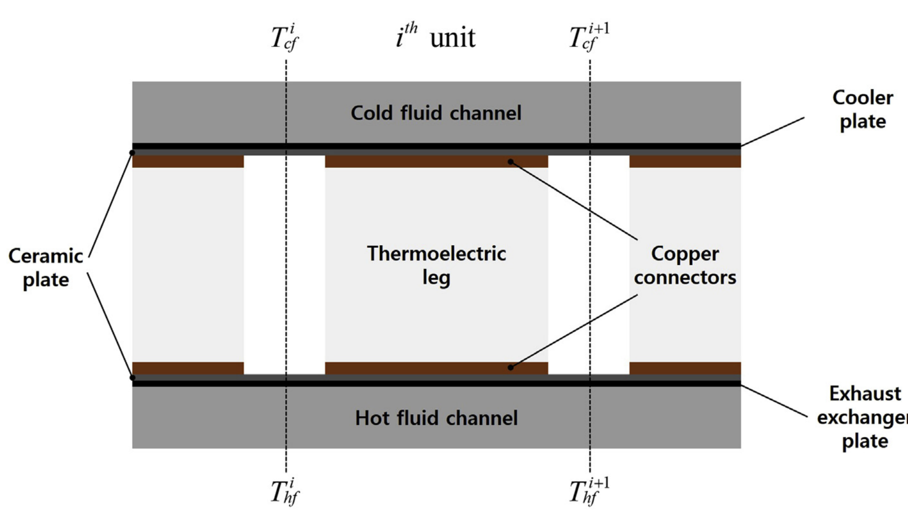

Fig. 3. Schematic representation of the TEG system.

Table 1
Basic equations associated with TEG system model [40].

Descriptions		Equations
TEG power output		$P_{TEG} = 2(Q_{hs} - Q_{cs})$
		$Q_{hs} = \sum_{i=1}^{n_x} q_{hs}^i$
		$Q_{cs} = \sum_{i=1}^{n_x} q_{cs}^i$
Electrical current		$I = \frac{U}{R_{int} + R_{load}}$
		$U = \sum_{i=1}^{n_x} n_y \alpha_{pn} (T_{hs}^i - T_{cs}^i)$
Heat transfer in hot-side	Heat released from hot fluid	$q_{hs}^i = \frac{1}{2} c_{hf} m_{hf} (T_{hf}^i - T_{hf}^{i+1})$
	Heat transferred to hot-side surface of thermoelectric module from hot fluid	$q_{hs}^i = n_y A k_{hf} \left(\frac{T_{hf}^i + T_{hf}^{i+1}}{2} - T_{hs}^i \right)$
	Heat absorbed on the hot-side surface of thermoelectric module	$q_{hs}^i = n_y \left(\alpha_{pn} I T_{hs}^i + K_{pn} (T_{hs}^i - T_{cs}^i) - \frac{1}{2} I^2 R_{pn} \right)$
	Convection heat transfer coefficient	$h_{hf} = \frac{Nu_{hf} \lambda_{hf}}{D_{hf}}$
	Total heat transfer coefficient	$k_{hf} = \left(\frac{1}{h_{hf}} + \frac{t_{exc}}{\lambda_{exc}} + \frac{t_{con}}{\lambda_{con}} + \frac{t_{cer}}{\lambda_{cer}} + R_{cont} \right)^{-1}$
Heat transfer in cold-side	Heat absorbed by cold fluid	$q_{cs}^i = \frac{1}{2} c_{cf} m_{cf} (T_{cf}^{i+1} - T_{cf}^i)$
	Heat transferred to cold fluid from cold-side surface of thermoelectric module	$q_{cs}^i = n_y A k_{cf} \left(T_{cs}^i - \frac{T_{cf}^i + T_{cf}^{i+1}}{2} \right)$
	Heat released on the cold-side surface of thermoelectric module	$q_{cs}^i = n_y \left(\alpha_{pn} I T_{cs}^i + K_{pn} (T_{hs}^i - T_{cs}^i) + \frac{1}{2} I^2 R_{pn} \right)$
TEG net power output		$P_{net} = P_{TEG} - P_{pump}$
		$P_{pump} = f_z \left(\frac{m_{hf}}{\rho_{hf}} \right)$
		$f_z = 4f \left(\frac{L}{D_{hf}} \right) \left(\frac{\rho_{hf} v_{hf}^2}{2} \right)$

Table 2
Basic parameters related to TEG system model.

Thermoelectric leg parameters		
Seebeck coefficient (VK^{-1})	P-type	2.037×10^{-4}
	N-type	-1.721×10^{-4}
Resistivity (Ωm)	P-type	1.314×10^{-5}
	N-type	1.119×10^{-5}
Thermal conductivity ($Wm^{-1}K^{-1}$)	P-type	1.265
	N-type	1.011
Semiconductor leg length/width/height (mm)	P-type	5/5/5
	N-type	5/5/5
Heat transfer parameters		
Thermal conductivity ($Wm^{-1}K^{-1}$)	Exchanger plate	398
	Ceramic plate	35
	Copper connector	398
Contact thermal resistance (m^2KW^{-1})	Exchanger plate	0.0005
Convective heat transfer coefficient ($Wm^{-2}K^{-1}$)	Cold fluid	1000

$\mathbf{e} = [e(\mathbf{x}_1),\ e(\mathbf{x}_2), \ldots,\ e(\mathbf{x}_n)]^T$ is a vector of stochastic process $e(\mathbf{x})$, which has a zero mean and covariance structure; and nr indicates the number of random variables plus random parameters.

In the covariance structure of the stochastic process, the model inputs are $(\mathbf{x}_i, \mathbf{x}_j)$ and the model outputs are the covariance of the outputs resulting from the inputs. The general idea of the covariance function assumes that the outputs of inputs that are close to each other are highly correlated, allowing different distance measures for each input dimension by using $\boldsymbol{\theta}$ as the parameters. Thus, the covariance structure of the stochastic process can be represented by the process variance σ^2, which can be derived after obtaining the optimum $\boldsymbol{\theta}$, and the user-defined correlation function $R(\boldsymbol{\theta}, \mathbf{x}_i, \mathbf{x}_j)$, as

$$\mathrm{cov}[e(\mathbf{x}_i), e(\mathbf{x}_j)] = \sigma^2 R(\boldsymbol{\theta}, \mathbf{x}_i, \mathbf{x}_j), \tag{3}$$

where $\boldsymbol{\theta} = (\theta_1,\ \theta_2, \ldots,\ \theta_{nr})$ is the vector of the unknown correlation parameters that will be estimated. The correlation function is a user-defined function and constitutes the correlation matrix $\mathbf{R}$, whose component is $R_{ij} = R(\boldsymbol{\theta}, \mathbf{x}_i, \mathbf{x}_j)$. The correlation function is formulated to reflect the decrease in the effect of the response function as the distance between the two sample points increases, and the influence of this distance can be changed by adjusting $\boldsymbol{\theta}$. In engineering applications, a Gaussian spatial correlation function is usually used as the correlation function. It is given by

$$R\left(\boldsymbol{\theta}, \mathbf{x}_i, \mathbf{x}_j\right) = \prod_{l=1}^{nr} \exp\left(-\theta_l \left(x_i^l - x_j^l\right)^2\right), \tag{4}$$

where θ_l, x_i^l, and x_j^l indicate the lth component of vectors $\boldsymbol{\theta}$, $\mathbf{x}_i$, and $\mathbf{x}_j$, respectively. The optimal $\boldsymbol{\theta}$ can be estimated from the maximum likelihood estimation, which maximizes the likelihood function f_L, given as

$$f_L = \left(2\pi\sigma^2\right)^{-\frac{n}{2}} |\mathbf{R}|^{-\frac{1}{2}} \exp\left[-\frac{1}{2\sigma^2}(\mathbf{Y} - \mathbf{F}\boldsymbol{\beta})^{\mathrm{T}}\mathbf{R}^{-1}(\mathbf{Y} - \mathbf{F}\boldsymbol{\beta})\right]. \tag{5}$$

The response at the point of interest $\mathbf{x}_0$ is predicted using a linear predictor of the Kriging method, as

$$\widehat{Y}(\mathbf{x}_0) = \mathbf{w}(\mathbf{x}_0)^{\mathrm{T}}\mathbf{Y}, \tag{6}$$

where $\mathbf{w}(\mathbf{x}_0)$ is an $n \times 1$ weight vector that consists of functions of $\mathbf{x}_0$. The unbiasedness condition $E[\widehat{Y}(\mathbf{x}_0)] = E[Y(\mathbf{x}_0)]$ can be expressed as

$$\begin{aligned} E[\widehat{Y}(\mathbf{x}_0) - Y(\mathbf{x}_0)] &= E\left[\mathbf{w}(\mathbf{x}_0)^{\mathrm{T}}\mathbf{Y} - Y(\mathbf{x}_0)\right] \\ &= E\left[\mathbf{w}(\mathbf{x}_0)^{\mathrm{T}}(\mathbf{F}\boldsymbol{\beta} + \mathbf{e}) - (\mathbf{f}_0\boldsymbol{\beta} + e(\mathbf{x}_0))\right] \\ &= E\left[\left(\mathbf{F}^{\mathrm{T}}\mathbf{w}(\mathbf{x}_0) - \mathbf{f}_0^{\mathrm{T}}\right)^{\mathrm{T}}\boldsymbol{\beta}\right] = 0 \end{aligned} \tag{7}$$

where $\mathbf{f}_0 = [f_1(\mathbf{x}_0),\ f_2(\mathbf{x}_0),\ \ldots, f_P(\mathbf{x}_0)]$. Therefore, the constraint $\mathbf{F}^{\mathrm{T}}\mathbf{w}(\mathbf{x}_0) = \mathbf{f}_0^{\mathrm{T}}$ can be derived and the mean squared error at the point of interest $\mathbf{x}_0$ can be given as

$$\begin{aligned} \mathrm{MSE}\left[\widehat{Y}\right] &= E\left[\left(\widehat{Y}(\mathbf{x}_0) - Y(\mathbf{x}_0)\right)^2\right] \\ &= \sigma^2\left(1 + \mathbf{w}(\mathbf{x}_0)^{\mathrm{T}}\mathbf{R}\mathbf{w}\left(\mathbf{x}_0\right) - 2\mathbf{w}\left(\mathbf{x}_0\right)^{\mathrm{T}}\mathbf{r}\left(\mathbf{x}_0\right)\right) \end{aligned} \tag{8}$$

where $\mathbf{r}(\mathbf{x}_0) = [R(\boldsymbol{\theta}, \mathbf{x}_0, \mathbf{x}_1), \ldots,\ R(\boldsymbol{\theta}, \mathbf{x}_0, \mathbf{x}_n)]^{\mathrm{T}}$ indicates the correlation vector between the point of interest and the sample points. To solve the minimization problem of the mean squared error, the Lagrange multiplier can be applied with the constraint $\mathbf{F}^{\mathrm{T}}\mathbf{w}(\mathbf{x}_0) = \mathbf{f}_0^{\mathrm{T}}$, as

$$\begin{aligned} \Lambda = {} & \sigma^2\left(1 + \mathbf{w}(\mathbf{x}_0)^{\mathrm{T}}\mathbf{R}\mathbf{w}\left(\mathbf{x}_0\right) - 2\mathbf{w}\left(\mathbf{x}_0\right)^{\mathrm{T}}\mathbf{r}\left(\mathbf{x}_0\right)\right) \\ & + \boldsymbol{\lambda}\left(\mathbf{F}^{\mathrm{T}}\mathbf{w}\left(\mathbf{x}_0\right) - \mathbf{f}_0^{\mathrm{T}}\right), \end{aligned} \tag{9}$$

where Λ is the Lagrangian function and $\boldsymbol{\lambda}$ is the Lagrange multiplier. The weight vector can then be obtained from the derivative of the Lagrangian function Λ, as

$$\mathbf{w}(\mathbf{x}_0) = \mathbf{R}^{-1}\left(\mathbf{r}(\mathbf{x}_0) + \frac{1}{2\sigma^2}\mathbf{F}\boldsymbol{\lambda}\right). \tag{10}$$

Substituting $\mathbf{w}(\mathbf{x}_0)$ into Eq. (6) yields

$$\widehat{Y}(\mathbf{x}_0) = \mathbf{f}(\mathbf{x}_0)\boldsymbol{\beta} + \mathbf{r}(\mathbf{x}_0)^{\mathrm{T}}\mathbf{R}^{-1}(\mathbf{Y} - \mathbf{F}\boldsymbol{\beta}), \tag{11}$$

where $\boldsymbol{\beta} = (\mathbf{F}^{\mathrm{T}}\mathbf{R}^{-1}\mathbf{F})^{-1}\mathbf{F}^{\mathrm{T}}\mathbf{R}^{-1}\mathbf{Y}$ and $\sigma^2 = \frac{1}{n}(\mathbf{Y} - \mathbf{F}\boldsymbol{\beta})^{\mathrm{T}}\mathbf{R}^{-1}(\mathbf{Y} - \mathbf{F}\boldsymbol{\beta})$ can be obtained using the generalized least squares regression approach. A simple 2-D numerical example is shown in Appendix A to demonstrate how the method is applied to problems.

2.2.2. Model validation

Validating a surrogate model before it is used to replace a computationally intensive model is important. The cross-validation method is generally used to assess the accuracy of a surrogate model because no additional samples are needed [43]. The k-fold cross validation operation is shown in Fig. 4. In the k-fold cross validation method, n input-output pairs $(\mathbf{x}, y)$ constitute a data set, $S\{X, Y\}$, where y is the model response at the design sample point $\mathbf{x}$ and n is the total number of sample points. The data set is divided into k different subsets of an equal size; that is, $S\{X,Y\} = S_1\{X_1,Y_1\}$, $S_2\{X_2, Y_2\}$, …, $S_k\{X_k, Y_k\}$. Then, leaving one of the subsets as a validation data set, a surrogate model is built using k−1 subsets and the error is computed at the validation point. Every subset is used as validation data once and the process of calculating the error at each point is repeated k times. The accuracy of each surrogate model can be evaluated using the normalized root mean squared error (NRMSE) given by Ref. [44].

$$\mathrm{NRMSE} = \frac{\sqrt{\frac{1}{N_{test}}\sum_{i=1}^{N_{test}}(y_i - \widehat{y}_i)^2}}{\max(y_i) - \min(y_i)}, \tag{12}$$

where N_{test} is the number of validation points, y_i is the observed

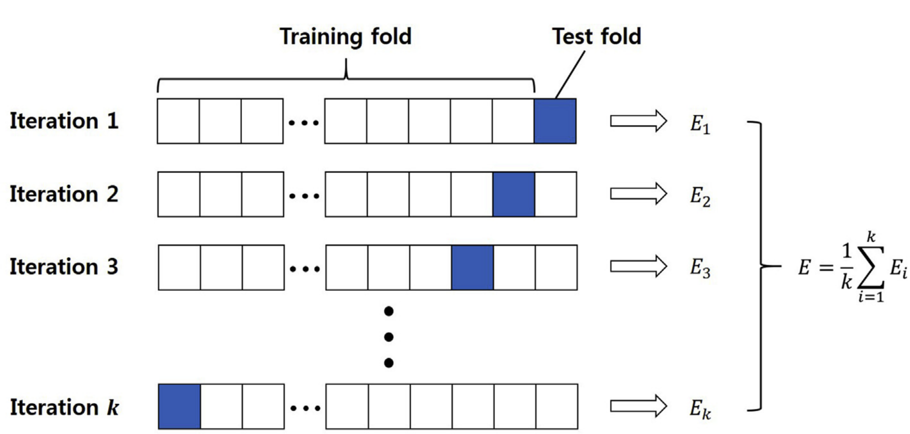

Fig. 4. Operation of k-fold cross validation.

value of the test fold samples, and $\hat{y}_i$ is the predicted response of the surrogate model created using the training fold samples. Finally, the accuracy of the surrogate model can be assessed using the average value of the NRMSE obtained from all surrogate models.

In this study, the TEG system model is approximated using a surrogate model with the following eight variables and parameters: the inlet temperature, total mass flow rate of the hot fluid, three dimensions of the heat exchanger (length, width, and height), the Seebeck coefficient, and the P-type and N-type electrical resistivity values. The surrogate model is constructed using 400 sample points obtained from the TEG system model simulation and the LHS method. Its NRMSE is 4.96%, which is reasonably accurate for use in engineering applications. In addition, the surrogate model is compared to numerical data of He [40]. The geometry of the TEG system of the referenced model is the sandwich type with a width of 0.8 m and height of 0.005 m, identical to that shown in Fig. 2. Hot and cold fluids flow in the same direction, and T_{ci}, T_{hi}, m_{cf}, and m_{hf} are 353.15K, 673.15K, 500gs^{-1}, and 46gs^{-1}, respectively. The accuracy of the referenced model is acceptable given that the comparison between the results of the referenced model and the experimental data shows small discrepancies. Fig. 5(a) and Fig. 5(b) show the comparison of the hot-side heat transfer coefficient and the TEG power output between the referenced data and the surrogate model, respectively. The comparison shows that the discrepancy between the surrogate and reference models is minor as well. The root mean square errors (RMSEs) of h_{hf}, P_{teg}, and P_{net} are 1.3024W/m^{-2}K^{-1}, 4.7934W, and 4.8408W, respectively. The discrepancies between the two models arise due to differences in the thermoelectric properties and the physical and material properties of the fluid and heat exchanger used in each model. Unlike the assumptions in the referenced model, changes in the thermoelectric properties with a temperature difference are considered in this study, and doing so contributes to the difference between the models. Moreover, the errors of the surrogate model itself affect the discrepancies.

2.3. Uncertainty in the TEG system model

Because variations of the material and physical properties of the thermoelectric material occur during the manufacturing process and given that TEG performances vary under different operating environments, unintended TEG output performances can arise [45]. Furthermore, some deviations in the exhaust parameters, such as the mass flow rate and exhaust gas temperature of the heat exchanger, lead to unintended output performance outcomes or large variations in the output performance [46]. Therefore, the uncertainties of the input parameters associated with the TEG system model should be quantified and considered in the TEG optimization to maximize the TEG performance while reducing its variances. The properties of uncertain parameters that can have a significant impact on the TEG net power output and its variation are referenced from the literature (shown in Table 3), and all distribution types are assumed to be normal. The mass flow rate and inlet temperature of the hot fluid can fluctuate depending on the engine operation, and the Seebeck coefficient and resistivity of the P—N semiconductor also vary due to differences in the material properties and errors attributed to the manufacturing process. The means of the total mass flow rate and inlet temperature of the hot fluid are assumed to be 40gs^{-1} and 873.15K, respectively, but a parametric study with various means of the total mass flow rate and inlet temperature of the hot fluid is conducted and the results are discussed in Section 4.

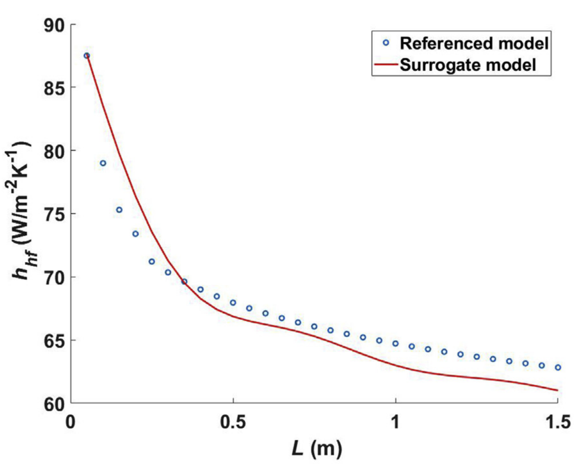

(a)

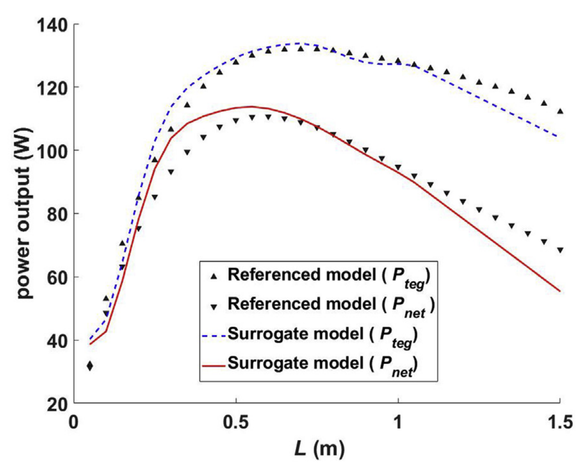

(b)

Fig. 5. Surrogate model validation through a comparison of (a) the heat transfer coefficient on the hot side and (b) the power output.

Table 3
Properties of uncertain parameters [20–22].

Uncertain parameter	Mean	COV[a]	Distribution type
Total mass flow rate of hot fluid (gs^{-1})	40	5%	Normal
Inlet temperature of hot fluid (K)	873.15	5%	Normal
Seebeck coefficient (VK^{-1})	3.758×10^{-4}	5%	Normal
P-type resistivity (Ωm)	1.314×10^{-5}	10%	Normal
N-type resistivity (Ωm)	1.119×10^{-5}	10%	Normal

[a] Coefficient of variation.

3. Methodologies for TEG optimization

3.1. Robust design optimization (RDO)

The conventional deterministic optimization is carried out without considering the uncertain factors of the variables and parameters; therefore, the deterministic optimum is sensitive to variations of the input variables and parameters. Thus, robustness of an objective function can be accomplished in RDO by maximizing the mean performance while minimizing its variance simultaneously. A conceptual comparison between deterministic and robust optimum is illustrated in Fig. 6, where the x-axis indicates a design variable or parameter with uncertainty and the y-axis indicates the performance function that should be minimized. Because the design variable or parameter has some variation, the corresponding performance function also varies. Compared to x_1, the slope of the performance function close to x_2 is relatively gentle, implying that the variation of the performance function is relatively small. With regard to simply minimizing the performance function, x_1 is considered to be optimized; however, the variation of the performance function (Δf_1) is large and thus the optimal performance cannot be guaranteed. On the other hand, though the optimum performance is not obtained in x_2, the variance of the performance function (Δf_2) is small and thus stable performance can be expected. Therefore, for the same variability in the design variable or parameter, the robust optimum (x_2) is less sensitive to input uncertainties and shows less variation in the performance than the deterministic optimum (x_1).

In this study, RDO is introduced for the design of the exhaust exchanger in the TEG system model, where the TEG net power output is maximized while minimizing the variance of the output with consideration of uncertain factors that affect the performance function. The uncertain parameters and deterministic design variables of the exhaust exchanger design problem are shown in Tables 3 and 4, respectively. The deterministic design variables L, W, H in Table 4 are identical to those in Fig. 2. In order to carry out the RDO, the objective function should contain the mean and variance

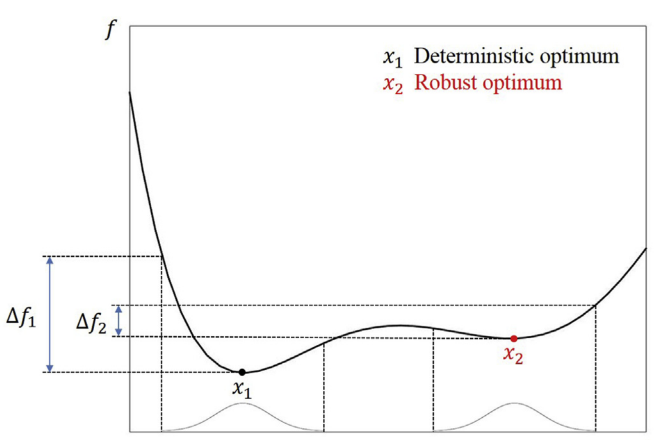

Fig. 6. Conceptual comparison between deterministic and robust optimization [47].

Table 4
Deterministic design variables.

Design variable	Lower bound	Upper bound
Total exchanger length (L)	0.05 m	2.00 m
Total exchanger width (W)	0.05 m	2.00 m
Total exchanger height (H)	0.002 m	0.01 m

of the performance function, with opposite signs. In addition, the mean and variance of the performance function should be normalized to prevent the problem caused by different scales, and each normalized mean and variance term has a weight that depends on its importance. Therefore, RDO for the exhaust exchanger in the TEG system model is formulated as

$$\max_{\mathbf{x}} \quad w_1\frac{\mu(\mathbf{P}_{net}(\mathbf{x},\mathbf{UP}))}{\mu(\mathbf{P}_{net}(\mathbf{x}_0,\mathbf{UP}))} - w_2\left(\frac{\sigma(\mathbf{P}_{net}(\mathbf{x},\mathbf{UP}))}{\sigma(\mathbf{P}_{net}(\mathbf{x}_0,\mathbf{UP}))}\right)^2 \qquad (13)$$
$$\text{subject to} \quad \mathbf{lb} \le \mathbf{x} \le \mathbf{ub}$$

where $\mathbf{x}$ indicates the deterministic design variable vector; $\mathbf{UP}$ denotes the uncertain parameter vector; $\mathbf{P}_{net}$ stands for TEG net power output vector; $\mu(\cdot)$ represents the mean value; $\sigma(\cdot)$ is the standard deviation; w_1 and w_2 correspond to weights of the mean and variance of $\mathbf{P}_{net}$, respectively; and $\mathbf{lb}$ and $\mathbf{ub}$ are correspondingly the lower bounds and upper bounds. The TEG net power output is defined as $P_{net} = P_{TEG} - P_{pump}$ and the initial deterministic design variables $\mu(\mathbf{P}_{net}(\mathbf{x}_0,\mathbf{UP}))$ and $\sigma(\mathbf{P}_{net}(\mathbf{x}_0,\mathbf{UP}))$ are used to normalize the two objectives.

3.2. Non-dominated sorting genetic algorithm II (NSGA-II)

As shown in Eq. (14), the RDO formulation has no single global solution because the optimization results vary depending on the weight setting. Thus, it is necessary to determine a set of trade-off optimal solutions [48]. The point $\mathbf{x}^*$ in design space $\mathbf{\Omega}$ is called a Pareto optimum if there exists no point $\mathbf{x}\in\mathbf{\Omega}$ such that $\mathbf{F}(\mathbf{x})$ dominates $\mathbf{F}(\mathbf{x}^*)$. All Pareto optimal solutions lie at the boundary of the feasible criterion space, and all Pareto optimal solutions comprise the Pareto set, which is also known as a Pareto front. The NSGA-II algorithm is one of the most popular multi-objective evolutionary algorithms for finding the Pareto set [49].

A schematic representation of the NSGA-II procedure for finding the Pareto set is shown in Fig. 7. In generation t, the parent population (P_t) and the offspring population (O_t) are combined to build a new population (R_t). To classify the population R_t into different non-dominated classes, fitness assignments are conducted by means of non-dominated sorting to create a number of fronts. An individual solution dominates other solutions when all objective functions are not worse than the other solutions and at least one objective function is better than the other solutions. During the fitness assignment process, solutions that are not dominated by any other solutions are given the highest fitness and assigned to the first front (F_1). The second front (F_2) is then assigned to solutions that are not dominated by solutions other than those in the first front. This process is repeated until fitness is assigned to all solutions. The selection is determined through tournament competition between two solutions and the selected solution is the one with the lowest front number. If both solutions are included in the same front, the selected solution is the one with the highest crowding distance; i.e., solutions located at a sparsely populated part of the front are assigned a higher fitness value to increase the diversity. This reproduction process occurs during each iteration, with each iteration having N parents and N newly generated offspring individuals. During each iteration, competition between 2N parents and offspring is conducted as presented in Fig. 7, and the iteration continues until the Pareto set is obtained.

The simulated binary crossover (SBX) and polynomial mutation methods are used in NSGA-II to generate the offspring population [50]. SBX generates two offspring from two parent solutions. The difference between a parent and an offspring is determined by the crossover index η_c. If η_c has a large value, 'near-parent' solutions have a higher probability of being selected as offspring, and distant

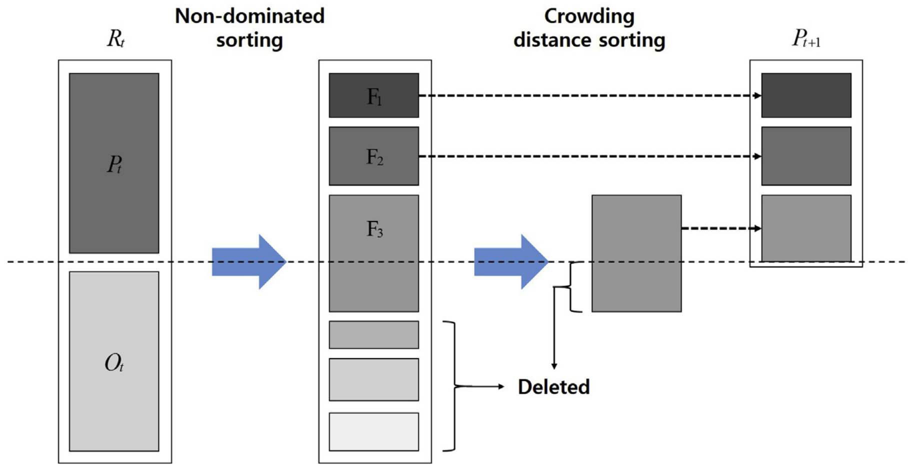

Fig. 7. Schematic representation of the NSGA-II procedure.

solutions are likely to be generated as offspring when η_c has a small value. The two generated offspring are symmetric about the parent solutions, and the two offspring show a spread proportional to that of the parents for a fixed η_c. The two properties of a spread are as follows: (a) there is a proportional relationship between the difference between the corresponding decision variables of the generated offspring and the difference between the corresponding decision variables of the parents; (b) offspring with decision variables closer to those of their parents have a better chance of being selected. A polynomial mutation indicates that the offspring near the parent are more likely to be generated than their distant counterparts. Throughout the iterations, the external parameter η_m remains constant and determines the probability distribution shape.

After obtaining the Pareto set, the utopia point method is used to select a single optimal solution. The utopia point $\mathbf{F}^0$ is defined as

$$\mathbf{F}^0 = \max_{\mathbf{x}}\{F_j(\mathbf{x})|\mathbf{x} \in \boldsymbol{\Omega}\} \qquad \text{s.t. } j \in \{1,\ 2,\ \ldots,\ C\}, \tag{14}$$

where $\mathbf{x}$ is the vector of the decision variable; F is an objective function; $\boldsymbol{\Omega}$ indicates all possible domains of the decision variable vector; and C is the number of objective functions. The utopia point cannot be obtained because there is a trade-off relationship between the objective functions, but it can still serve as a reference point. Then, a compromise solution can be derived by the distance minimization problem, as shown below.

$$\min_{\mathbf{x}} \quad \left\|\mathbf{F}(\mathbf{x}) - \mathbf{F}^0\right\|_p \qquad \text{s.t. } \mathbf{x} \in \boldsymbol{\Omega} \tag{15}$$

Here, $\|\cdot\|_p$ indicates the p-norm.

3.3. Global sensitivity analysis

Global sensitivity analysis is a term used to describe which input parameters have the greatest effect on the output performance function when uncertainty exists in the parameters [51]. The Sobol index is defined as a global sensitivity indicator that quantifies the effect of each uncertain model input on the output distribution. As shown in Fig. 1, a global sensitivity analysis using the Sobol index is performed to measure the impact of the input uncertainties of the TEG model on the TEG net power output. The Sobol method derives the Sobol index via the decomposition of the variance that decomposes the variance of the model output function into the sum of the variances affected by the input parameters of interest [52]. To obtain the Sobol index of the output performance function $y = f(\mathbf{x})$ considering the variation of input $\mathbf{x} = (x_1,\ x_2,\ \ldots,\ x_n)$, an input variable space $\boldsymbol{\Omega} = \{\mathbf{x}|x_i \in [0,\ 1];\ i = 1, \ldots, n\}$ is defined. Then, an integrable function $f(\mathbf{x})$ can be decomposed, as

$$f(\mathbf{x}) = f_0 + \sum_{i=1}^{n} f_i(x_i) + \sum_{i<j} f_{ij}(x_i,\ x_j) + \cdots + f_{12\cdots n}(x_1,\ x_2, \ldots,\ x_n). \tag{16}$$

This is referred to as an analysis of variance (ANOVA)-representation of $f(\mathbf{x})$ if

$$\int_0^1 f_{i_1\cdots i_s}(x_{i_1}, \ldots, x_{i_s})\mathrm{d}x_{i_k} = 0 \quad \text{for} \quad k = 1, \ldots, s. \tag{17}$$

The total variance V of $f(\mathbf{x})$ is then defined as

$$V = \int_{\Omega_n} f^2(\mathbf{x})\mathrm{d}\mathbf{x} - f_0^2, \tag{18}$$

where $\mathrm{d}\mathbf{x}$ is $\mathrm{d}x_1 \ldots \mathrm{d}x_n$, and the partial variances can be calculated as

$$V_{i_1\cdots i_s} = \int_0^1 \cdots \int_0^1 f^2_{i_1\cdots i_s}(x_{i_1}, \ldots, x_{i_s})\mathrm{d}x_{i_1}\cdots \mathrm{d}x_{i_s}. \tag{19}$$

Squaring Eq. (17) and integrating over the input variable space $\boldsymbol{\Omega}$ yields

$$V = \sum_{s=1}^{n} \sum_{i_1 < \cdots < i_s}^{n} V_{i_1\cdots i_s}. \tag{20}$$

Hence, the global sensitivity indices are defined by

$$S_{i_1\cdots i_s} = \frac{V_{i_1\cdots i_s}}{V}, \tag{21}$$

where the integer s indicates the order of the index.

For an arbitrary set of q variables derived from the total of n variables, $1 \le q \le n-1$, the set can be expressed as

$$\mathbf{b} = \left(x_{k_1}, \ldots, x_{k_q}\right), \qquad 1 \le k_1 < \cdots < k_q \le n \tag{22}$$

and let the set of complementary $n-q$ variables can be $\mathbf{c}$; thus, $\mathbf{x} = (\mathbf{b}, \mathbf{c})$. Let $\mathbf{Q} = (k_1, \ldots, k_q)$, with the variance of the subset $\mathbf{b}$ then defined as

$$V_{\mathbf{b}} = \sum_{s=1}^{q} \sum_{(i_1 < \cdots < i_s) \in \mathbf{Q}} V_{i_1 \cdots i_s}. \tag{23}$$

Similarly, the variance of $\mathbf{c}$ can be defined and the total variance of subset $\mathbf{b}$ can be derived as

$$V_{\mathbf{b}}^{total} = V - V_{\mathbf{c}}. \tag{24}$$

Therefore, for the subset $\mathbf{b}$, two global sensitivity indices are given as

$$S_{\mathbf{b}} = \frac{V_{\mathbf{b}}}{V}, \qquad S_{\mathbf{b}}^{total} = \frac{V_{\mathbf{b}}^{total}}{V} \tag{25}$$

where $S_{\mathbf{b}}^{total} = 1 - S_{\mathbf{c}}$ and $0 \le S_{\mathbf{b}} \le S_{\mathbf{b}}^{total} \le 1$.

4. Results and discussion

This section presents the results of the RDO and multi-objective optimization processes using NSGA-II as explained in Section 3 for the exhaust exchanger design in the TEG and the global sensitivity analysis of the uncertain parameters. For RDO as expressed by Eq. (13), SQP with various initial points is used. The Computation time for one optimization is on average 9 h with a regular desktop computer (Intel i7 6900 CPU @ 128.0 GB RAM and 3.20 GHz).

Table 5 presents the optimal outcomes and designs obtained using RDO with various weights. Each optimization result depends on the weights of the mean and variance of the TEG net power output. When w_1 is high, RDO focuses on maximizing the TEG net power output, whereas it focuses on minimizing the variance when w_2 is high.

The standard deviations of the TEG net power output in Table 5 show that the parameter uncertainties significantly affect the variation of the TEG net power output. Therefore, it is important to quantify the uncertain factors associated with the TEG system model and to perform optimization considering the uncertainty of the parameters. The deterministic optimum is the optimum design found without considering the variation of the performance function caused by the uncertainty of the parameters, and this optimum represents the design that can be derived from existing studies on TEG optimization. During the operation of the actual TEG, the RDO optimum designs derived from various weight combinations all have less variation of the TEG net power output than the deterministic optimum design. Because the deterministic optimum design is derived without considering the uncertainties, the performance decreases and the variation can be significant when uncertainties exist during the actual operation of the device. A comparison of the RDO optimum design with the largest w_1 and the deterministic optimum design shows that the mean of the TEG net power output of the RDO optimum design increases by 37.6% while the standard deviation decreases by 34.9%. For the mean of the TEG net power output to be larger in the RDO optimum design than in the deterministic optimum design, the boundary value of w_1 is 0.4. A comparison of the RDO optimum design at this boundary value and the deterministic optimum design shows that the mean of the TEG net power output of the RDO optimum design increases by 10.4% while the standard deviation decreases by 65.0%. As w_2 increases, the mean and standard deviation of the output decrease at the same time. If w_2 is larger than w_1, the mean of the output decreases drastically, and is not applicable in reality. As w_2 increases, L tends to increase. However, when w_2 is larger than w_1, L begins to decrease to reduce the standard deviation even if the mean of the output decreases. In addition, as w_2 increases, the perimeter of the heat exchanger section − $2 \times (W+H)$ − becomes large to reduce influence of the variation of the total mass flow rate by reducing the velocity of the flow.

Table 6 presents the results of a parametric study conducted varying the COV of the total mass flow rate (m_{hf}) and the inlet temperature of the hot fluid (T_{hi}). It can be seen in Table 6 that with the deterministic optimum design, the mean and standard deviation of the TEG net power output are influenced more by the inlet temperature than by the total mass flow rate. Crane [19] reported that a 1% change in the initial fluid temperature could cause a 15% difference in the power output under certain conditions. The results of He [46] also showed that changes in the gas intake temperature have considerable effects on the power output.

In another parametric study, NSGA-II is utilized while varying the mean values of m_{hf} and T_{hi}, which are previously set to 40 gs^{-1}

Table 6
Mean and standard deviation at the deterministic optimum depending on COV of m_{hf} and T_{hi}.

COV		Mean (W)	Standard deviation (W)
m_{hf}	T_{hi}		
5%	5%	159.418	93.511
10%	5%	151.816	95.236
5%	10%	97.236	137.068
10%	10%	89.039	138.408

Table 5
Mean, standard deviation, and optimum design depending on weights ($m_{hf} = 40\text{gs}^{-1}$, $T_{hi} = 873.15\text{K}$).

w_1	w_2	$\mu_{P_{net}}$ (W)	$\sigma_{P_{net}}$ (W)	L (m)	W (m)	H (m)
1.0	0.0	219.44	60.85	7.481×10^{-1}	7.228×10^{-1}	5.126×10^{-3}
0.9	0.1	219.21	58.46	8.335×10^{-1}	7.238×10^{-1}	5.226×10^{-3}
0.8	0.2	218.01	55.43	8.928×10^{-1}	7.367×10^{-1}	5.375×10^{-3}
0.7	0.3	216.37	53.35	9.253×10^{-1}	7.464×10^{-1}	5.502×10^{-3}
0.6	0.4	213.25	50.91	9.466×10^{-1}	7.583×10^{-1}	5.664×10^{-3}
0.5	0.5	205.63	46.74	9.538×10^{-1}	7.580×10^{-1}	5.864×10^{-3}
0.4	0.6	176.07	32.69	8.061×10^{-1}	8.725×10^{-1}	5.916×10^{-3}
0.3	0.7	156.95	23.12	7.561×10^{-1}	9.225×10^{-1}	6.172×10^{-3}
0.2	0.8	145.06	17.84	7.251×10^{-1}	9.623×10^{-1}	6.373×10^{-3}
0.1	0.9	135.78	15.65	6.912×10^{-1}	10.04×10^{-1}	6.475×10^{-3}
Deterministic optimum		159.42	93.51	8.582×10^{-1}	2.288×10^{-1}	7.915×10^{-3}

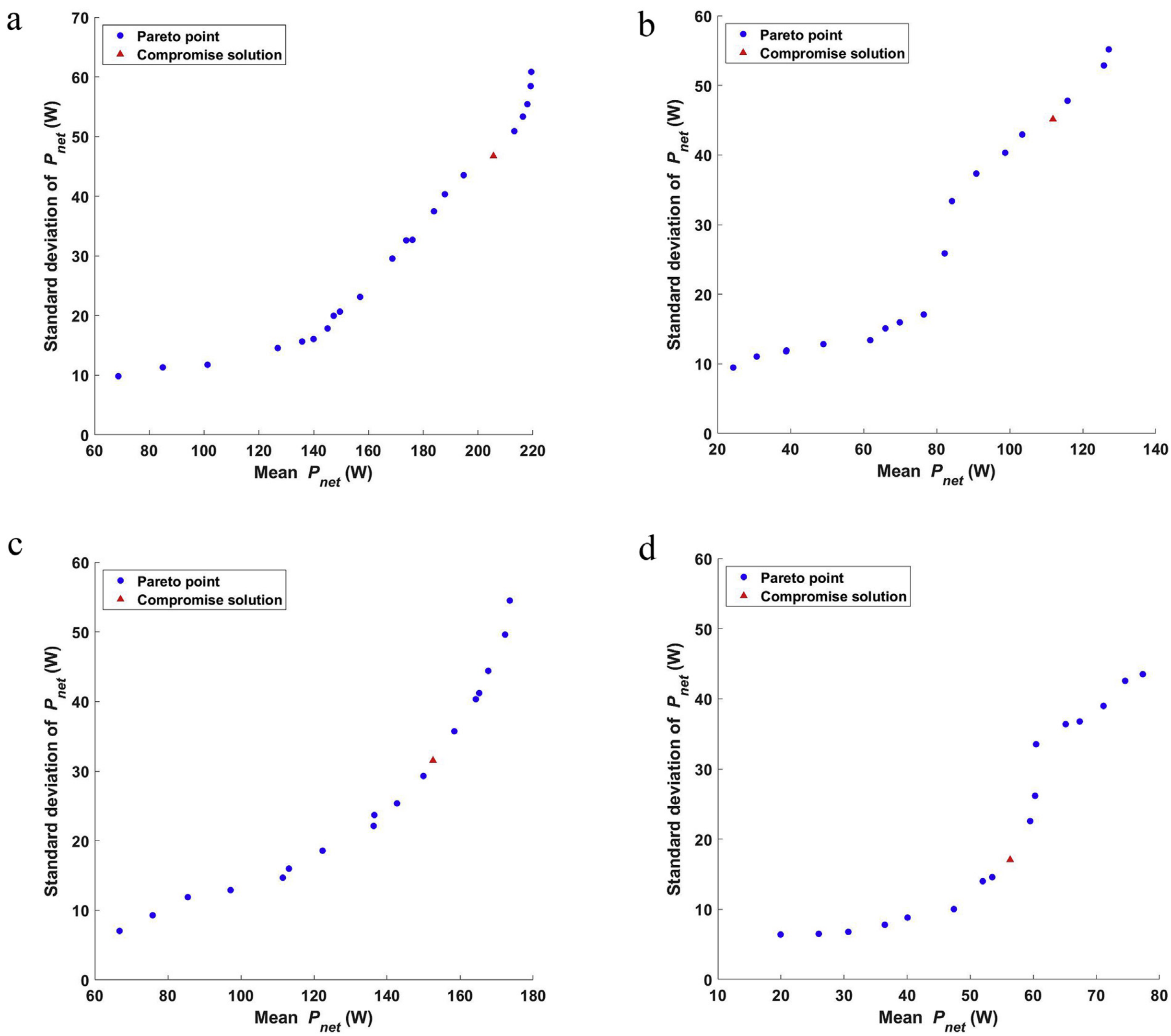

Fig. 8. Pareto front obtained using various means of m_{hf} and T_{hi}.

Table 7
Compromise solutions obtained using various means of m_{hf} and T_{hi}.

m_{hf} (gs^{-1})	T_{hi} (K)	$\mu_{P_{net}}$ (W)	$\sigma_{P_{net}}$ (W)	L (m)	W (m)	H (m)
40	873.15	205.63	46.74	9.538×10^{-1}	7.850×10^{-1}	5.864×10^{-3}
40	673.15	111.84	45.15	6.956×10^{-1}	6.357×10^{-1}	6.793×10^{-3}
30	873.15	152.59	31.53	7.099×10^{-1}	4.958×10^{-1}	7.600×10^{-3}
30	673.16	56.32	17.07	13.74×10^{-1}	2.715×10^{-1}	8.868×10^{-3}

and 873.15K, respectively, while fixing their COVs at 5% in both cases. Fig. 8 presents the Pareto front obtained from the parametric study. The mean of the TEG net power output at the Pareto front tends to decrease as the means of m_{hf} and T_{hi} decrease. However, the mean of the TEG net power output at the Pareto front is more affected by changes in the mean of T_{hi} than by the mean of m_{hf}.

The trade-off relationship between the mean and standard deviation of the TEG net power output at the Pareto front is important in heat exchanger design. Considering this trade-off relationship, compromise solutions obtained using various means of m_{hf} and T_{hi} are listed in Table 7, which shows that accurate uncertainty quantification is important when there are variations of m_{hf} and T_{hi}. When the mean of m_{hf} is 40 gs^{-1} and the mean of T_{hi} changes from 873.15K to 673.15K, H increases by 19.9% while L and W decrease by 26.5% and 16.2%, respectively. Similarly, when the mean of T_{hi} is 873.15K and the mean of m_{hf} changes from 40 gs^{-1} to 30 gs^{-1}, H increases by 33.6% while L and W decrease by 24.7% and 41.9%, respectively. However, when the mean of both m_{hf} and T_{hi} change correspondingly from 40 gs^{-1} and 873.15K to 30 gs^{-1} and 673.15K, W decreases by 64.2%, while L and H increase by 45.2% and 56.6%, respectively, showing a different tendency from the cases above. Because the TEG system model has considerable nonlinearity, the accuracy of uncertainty quantification has a significant influence on the design of the heat exchanger. When the mean values of m_{hf} and T_{hi} are 40 gs^{-1} and 873.15K, respectively, a comparison of the compromise solution and the deterministic optimum design shows that the mean of the TEG net power output of the compromise solution increases by 25.6% while the standard deviation decreases by 49.2%.

The global sensitivity analysis of the uncertain parameters is

Table 8
Sobol index of uncertain parameters.

	m_{hf}	T_{hi}	Seebeck coefficient	P-type resistivity	N-type resistivity
Sobol index	0.419	0.639	0.218	0.116	0.072

conducted using the Sobol method, as explained in Section 3.3, and these results are shown in Table 8. Similar to the results of the parametric study in Table 6, the Sobol index of T_{hi} is largest, meaning that it has the greatest effect on the TEG net power output. The Sobol index of m_{hf} is second largest, and the Sobol index of the Seebeck coefficient is largest among the uncertain parameters related to the thermoelectric properties.

5. Conclusion

In this study, uncertain factors of the TEG system model are considered and RDO is introduced into the heat exchanger optimization problem to derive a design that can reduce the variation of the TEG net power output. The COV of the TEG net power output with the deterministic optimum design is 56.2%, indicating that the uncertain parameters related to the TEG system model have a considerable influence on the variation of the power output. These results indicate that the accurate uncertainty quantification is essential in the TEG optimization problem. The RDO results show that it is important to obtain an optimal heat exchanger design after determining appropriate weights of the mean and standard deviation. The parametric study results with various means of the total mass flow rate and inlet temperature of the hot fluid show that the Pareto front and the optimal design vary depending on the total mass flow rate and inlet temperature. Thus, a compromise solution for the given total mass flow rate and inlet temperature of the hot fluid can be found from the Pareto front obtained from NSGA-II. When the mean values of m_{hf} and T_{hi} are 40 gs^{-1} and 873.15K, respectively, the COV of the TEG net power output of the compromise solution decreases by 33.5% point compared to the deterministic optimum design. A comparison of the compromise solution and the deterministic optimum design shows that the mean of the TEG net power output of the compromise solution increases by 25.6% while the standard deviation decreases by 49.2%. These results indicate that the compromise solution guarantees stable and high TEG net power output compared to the deterministic optimum design. A global sensitivity analysis of the uncertain parameters of the TEG system model was conducted using the Sobol method, with the results indicating that the Sobol index of the inlet temperature of the hot fluid (0.639) is largest, meaning that the inlet temperature is the most important factor affecting the TEG net power output. The Sobol index of the Seebeck coefficient (0.218) is largest among the uncertain parameters associated with the thermoelectric properties.

Acknowledgment

This work was supported by a project focusing on the development of a thermoelectric power generation system and business model utilizing non-use heat in industry funded by the Korea Institute of Energy Technology Evaluation and Planning (KETEP) and by the Ministry of Trade Industry & Energy (MOTIE) of the Republic of Korea (No. 20172010000830).

Appendix A. Numerical example of the Kriging method

This section shows how the Kriging method is applied to problems. The Branin-Hoo function, given by

$$f(x_1,x_2)=\left[x_2-\left(\frac{5.1}{4\pi^2}\right)x_1^2+\left(\frac{5}{\pi}\right)x_1-6\right]^2+10\left(1-\frac{1}{8\pi}\right)\cos x_1+10,\ x_1\in[-5,\ 10],\ x_2\in[0,\ 15] \tag{A.1}$$

is used as a numerical example. To build a surrogate model of the Branin-Hoo function, LHS is used to generate 20 samples, as presented in Table A1, and the sample points and responses are normalized using the means and standard deviations. A second-order polynomial regression function is used as the basis function. To solve the maximum likelihood estimation with the likelihood function L in Eq. (5), $\boldsymbol{\beta}=(\mathbf{F}^{\mathrm{T}}\mathbf{R}^{-1}\mathbf{F})^{-1}\mathbf{F}^{\mathrm{T}}\mathbf{R}^{-1}\mathbf{Y}$, and $\sigma^2=\frac{1}{n}(\mathbf{Y}-\mathbf{F}\boldsymbol{\beta})^{\mathrm{T}}\mathbf{R}^{-1}(\mathbf{Y}-\mathbf{F}\boldsymbol{\beta})$, the minimization problem for $\boldsymbol{\theta}$ can be expressed as

$$\min_{\boldsymbol{\theta}}\quad \ln\left(\sigma^2\right)+\ln(|\mathbf{R}|)^{\frac{1}{20}}. \tag{A.2}$$

The optimum solution, the regression coefficients, and the process variance can then be obtained as $\boldsymbol{\theta}=[2.3784,\ 0.2293]$, $\boldsymbol{\beta}=[0.0458,\ 0.0528,\ 0.5256,\ -0.1665,\ 0.7404,\ 0.3651]^{\mathrm{T}}$, and $\sigma^2=572.4778$, respectively. The NRMSE calculated from the cross-validation step is 1.4414. A 3D plot and a contour plot with sample points of the Branin-Hoo function and the surrogate model are shown in Fig. A1.

Table A.1
20 sample points generated using LHS

No.	1	2	3	4	5	6	7	8	9	10
x_1	6.535	−3.211	0.158	1.657	2.287	7.948	5.192	7.128	2.549	9.701
x_2	1.428	14.955	2.385	1.671	3.603	0.079	6.237	9.257	12.757	12.725
$f(\mathbf{x})$	19.395	6.728	30.815	13.358	4.020	11.149	39.603	80.985	101.525	100.904
No.	11	12	13	14	15	16	17	18	19	20
x_1	−4.289	3.572	−1.811	0.760	5.880	−2.166	4.046	−0.862	8.845	−3.666
x_2	10.932	7.883	10.062	14.188	8.505	5.961	11.582	4.716	4.134	7.037
$f(\mathbf{x})$	24.299	36.306	8.291	103.866	73.545	21.368	102.205	23.823	6.397	44.374

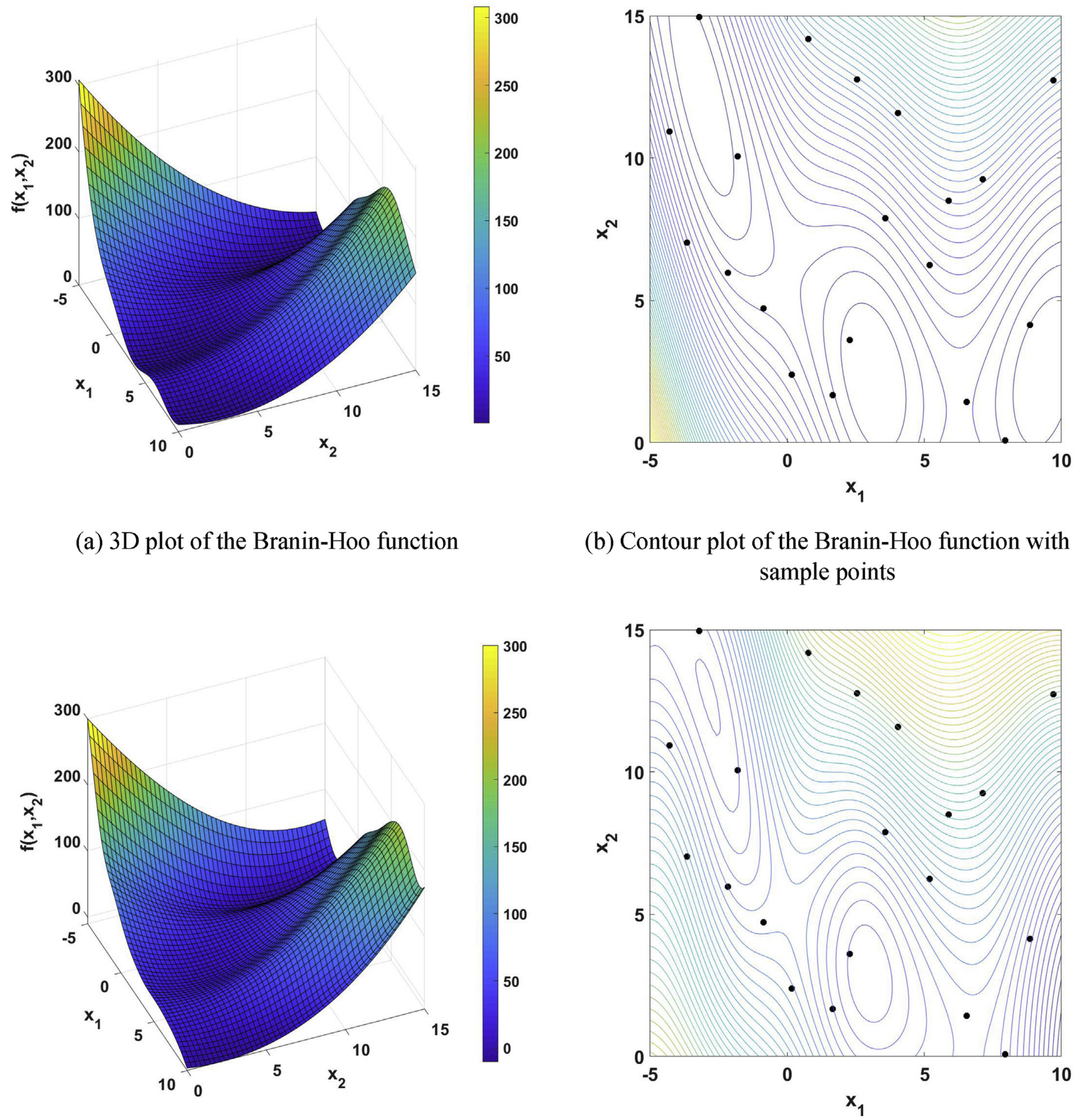

(a) 3D plot of the Branin-Hoo function

(b) Contour plot of the Branin-Hoo function with sample points

(c) 3D plot of the surrogate model

(d) Contour plot of the surrogate model with sample points

Fig. A.1. Plots of the Branin-Hoo function and the surrogate model.

References

[1] Höök M, Tang X. Depletion of fossil fuels and anthropogenic climate change — a review. Energy Pol 2013;52:797—809.

[2] Hsiao Y, Chang W, Chen S. A mathematic model of thermoelectric module with applications on waste heat recovery from automobile engine. Energy 2010;35:1447—54.

[3] Meng J, Wang X, Chen W. Performance investigation and design optimization of a thermoelectric generator applied in automobile exhaust waste heat recovery. Energy Convers Manag 2016;120:71—80.

[4] Gou X, Xiao H, Yang S. Modeling, experimental study and optimization on low-temperature waste heat thermoelectric generator system. Appl Energy 2010;87:3131—6.

[5] Ji D, Wei Z, Mazzoni S, Mengarelli M, Rajoo S, Zhao J, et al. Thermoelectric generation for waste heat recovery: application of a system level design optimization approach via Taguchi method. Energy Convers Manag 2018;172: 507—16.

[6] Domingues A, Santos H, Costa M. Analysis of vehicle exhaust waste heat recovery potential using a Rankine cycle. Energy 2013;49:71—85.

[7] Zhang Y, Cleary M, Wang X, Kempf N, Schoensee L, Yang J, et al. High-temperature and high-power-density nanostructured thermoelectric generator for automotive waste heat recovery. Energy Convers Manag 2015;105: 946—50.

[8] Lan S, Yang Z, Chen R, Stobart R. A dynamic model for thermoelectric

generator applied to vehicle waste heat recovery. Appl Energy 2018;210: 327–38.
[9] Nithyanandam K, Mahajan RL. Evaluation of metal foam based thermoelectric generators for automobile waste heat recovery. Int J Heat Mass Tran 2018;122:877–83.
[10] Muralidhar N, Himabindu M, Ravikrishna RV. Modeling of a hybrid electric heavy duty vehicle to assess energy recovery using a thermoelectric generator. Energy 2018;148:1046–59.
[11] Zhao Y, Wang S, Ge M, Liang Z, Liang Y, Li Y. Performance investigation of an intermediate fluid thermoelectric generator for automobile exhaust waste heat recovery. Appl Energy 2019;239:425–33.
[12] Deng YD, Liu X, Chen S. Thermal optimization of the heat exchanger in the automotive exhaust based thermoelectric generator. J Electron Mater 2013;42:1634–40.
[13] Liang X, Sun X, Tian H, Shu G, Wang Y, Wang X. Comparison and parameter optimization of a two-stage thermoelectric generator using high temperature exhaust of internal combustion engine. Appl Energy 2014;130:190–9.
[14] Su CQ, Wang WS, Liu X, Deng YD. Simulation and experimental study on thermal optimization of the heat exchanger for automotive exhaust-based thermoelectric generators. Case Stud Therm Eng 2014;4:85–91.
[15] Kumar S, Heister SD, Xu X, Salvador JR. Optimization of thermoelectric components for automobile waste heat recovery systems. J Electron Mater 2015;44:3627–36.
[16] Kempf N, Zhang Y. Design and optimization of automotive thermoelectric generators for maximum fuel efficiency improvement. Energy Convers Manag 2016;121:224–31.
[17] Chen WH, Wu PH, Lin YL. Performance optimization of thermoelectric generators designed by multi-objective genetic algorithm. Appl Energy 2018;209: 211–23.
[18] Marvão A, Coelho PJ, Rodrigues HC. Optimization of a thermoelectric generator for heavy-duty vehicles energy. Convers Manag 2019;179:178–91.
[19] Crane DT, Jackson GS. Optimization of cross flow heat exchangers for thermoelectric waste heat recovery. Energy Convers Manag 2004;45:1565–82.
[20] Prasad RC, Bharadwaj KK. Stochastic modeling of heat exchanger response to data uncertainties. Appl Math Model 2002;26:715–26.
[21] Casali D. Uncertainty quantification in pipe flow systems. Ms. thesis. 2013.
[22] Borup KA, Boor JD, Wang H, Drymiotis F, Gascoin F, Shi X, et al. Measuring thermoelectric transport properties of materials. Energy Environ Sci 2015;8: 423–35.
[23] Wang H, Porter WD, Böttner H, König J, Chen L, Bai S, et al. Transport properties of bulk thermoelectrics: an international round-robin study, Part I: seebeck coefficient and electrical resistivity. J Electron Mater 2013;42: 654–64.
[24] Frangopol DM, Maute K. Life-cycle reliability-based optimization of civil and aerospace structures. Comput Struct 2003;81:397–410.
[25] Youn BD, Choi KK, Yang RJ, Gu L. Reliability-based design optimization for crashworthiness of vehicle side impact. Struct Multidiscip Optim 2004;26: 272–83.
[26] Shin J, Lee I. Reliability-based vehicle safety assessment and design optimization of roadway radius and speed limit in windy environments. J Mech Des 2014;8:1006–19.
[27] Lee U, Kang N, Lee I. Selection of optimal target reliability in RBDO through reliability-based design for market systems (RBDMS) and application to electric vehicle design. Struct Multidiscip Optim 2019:1–15.
[28] Lee I, Choi KK, Du L, Gorsich D. Dimension reduction method for a reliability-based robust design optimization. Comput Struct 2008;86:1550–62.
[29] Kang Z, Bai S. On robust design optimization of truss structures with bounded uncertainties. Struct Multidiscip Optim 2013;47:699–714.
[30] Fang J, Gao Y, Sun G, Xu C, Li Q. Multiobjective robust design optimization of fatigue life for a truck cab. Reliab Eng Syst Saf 2014;135:1–8.
[31] Tammareddi S, Sun GY, Li Q. Multiobjective robust optimization of coronary stents. Mater Des 2016;90:682–92.
[32] Wu X, Zhang W, Song S. Robust aerodynamic shape design based on an adaptive stochastic optimization framework. Struct Multidiscip Optim 2017;3:1–13.
[33] Kang Z, Wu CL, Luo YJ, Li M. Robust topology optimization of multi-material structures considering uncertain graded interface. Compos Struct 2019;208: 395–406.
[34] Chandra MJ. Statistical quality control. Florida: CRC Press; 2001.
[35] Rubinstein RY. Simulation and the Monte Carlo method. New York: Wiley; 1981.
[36] Helton JC, Davis FJ. Latin hypercube sampling and the propagation of uncertainty in analyses of complex systems. Reliab Eng Syst Saf 2003;81:23–69.
[37] Zhang K, Han Z, Li W, Song W. Coupled aerodynamic/structural optimization of a subsonic-transport wing using surrogate model. J Aircraft 2008;45: 2167–70.
[38] Samad A, Lee KD, Kim KY. Shape optimization of a dimpled channel to enhance heat transfer using a weighted-average surrogate model. Heat Tran Eng 2010;31:1114–24.
[39] Li H, Liu T, Wang M, Zhao D, Qiao A, Wang X, et al. Design optimization of stent and its dilatation balloon using kriging surrogate model. Biomed Eng Online 2017;16:1–17.
[40] He W, Wang S, Yue L. High net power output analysis with changes in exhaust temperature in a thermoelectric generator system. Appl Energy 2017;196: 259–67.
[41] He W, Wang S, Yang Y. Peak power evaluation and optimal dimension design of exhaust heat exchanger for different gas parameters in automobile thermoelectric generator. Energy Convers Manag 2017;151:661–9.
[42] Kang K, Qin C, Lee B, Lee I. Modified screening-based Kriging method with cross validation and application to engineering design. Appl Math Model 2019;70:626–42.
[43] Wang G, Shan S. Review of metamodeling techniques in support of engineering design optimization. J Mech Des 2007;129:370–80.
[44] Zhang J, Chowdhury S, Messac A. An adaptive hybrid surrogate model. Struct Multidiscip Optim 2012;46:223–38.
[45] Lowhorn ND, Wong-Ng w, Zhang w, Lu ZQ, Otani M, Thomas E, et al. Round-robin studies of two potential seebeck coefficient standard reference materials. In: 26th International Conference of Thermoelectrics. IEEE, Jeju Island, South Korea; 2007. p. 361–5. 2007.
[46] He W, Wang S, Zhang X, Li Y, Lu C. Optimization design method of thermoelectric generator based on exhaust gas parameters for recovery of engine waste heat. Energy 2015;91:1–9.
[47] Augusto OB, Bennis F, Caro S. Multiobjective engineering design optimization problems: a sensitivity analysis approach. Pesqui Oper 2012;32:575–96.
[48] Deb K. Multi-objective optimization using evolutionary algorithms. New York: Wiley; 2001.
[49] Deb K, Pratap A, Agarwal S, Meyarivan T. A fast and elitist multiobjective genetic algorithm: NSGA-II. IEEE Trans Evol Comput 2002;6:182–97.
[50] Deb K, Agrawal RB. Simulated binary crossover for continuous search space. Complex Syst 1995;9:115–48.
[51] Lee K, Cho H, Lee I. Variable selection using Gaussian process regression-based metrics for high-dimensional model approximation with limited data. Struct Multidiscip Optim 2018:1–16.
[52] Sobol IM. Global sensitivity indices for nonlinear mathematical models and their Monte Carlo estimates. Math Comput Simulat 2001;55:271–80.